

## Article

# Assessing the Performance of Continuous-Flow Microbial Fuel Cells and Membrane Electrode Assembly with Electrodeposited Mn Oxide Catalyst

Laura Mais , Michele Mascia \*  and Annalisa Vacca 

Dipartimento di Ingegneria Meccanica, Chimica e dei Materiali, Università degli Studi di Cagliari, Via Marengo 2, 09123 Cagliari, Italy; laura.mais@unica.it (L.M.); annalisa.vacca@unica.it (A.V.)

\* Correspondence: michele.mascia@unica.it

**Abstract:** Microbial fuel cells (MFCs) are considered promising energy sources whereby chemical energy is converted into electricity via bioelectrochemical reactions utilizing microorganisms. Several factors affect MFC performance, including cathodic reduction of oxygen, electrode materials, cell internal and external resistances, and cell design. This work describes the effect of the catalyst coating in the air-cathode membrane electrode assembly (MEA) for a microbial fuel cell (MFC) prepared via electrodeposition of manganese oxide. The characterization of the synthesized air-cathode MFC, operating in a continuous mode, was made via electrochemical impedance spectroscopy (EIS) analyses for the determination of the intrinsic properties of the electrode that are crucial for scalability purposes. EIS analysis of the MFCs and of the MEA reveals that the anode and cathode contribute to polarization resistance by about 85% and 15%, respectively, confirming the high catalytic activity of the Mn-based air cathode. The maximum power density of the Mn-based cathode is about 20% higher than that recorded using a Pt/C electrode.

**Keywords:** membrane electrode assembly; electrodeposited Mn oxide; flow microbial fuel cells; electrochemical impedance spectroscopy; oxygen reduction reaction



**Citation:** Mais, L.; Mascia, M.; Vacca, A. Assessing the Performance of Continuous-Flow Microbial Fuel Cells and Membrane Electrode Assembly with Electrodeposited Mn Oxide Catalyst. *Energies* **2024**, *17*, 943. <https://doi.org/10.3390/en17040943>

Academic Editor: Abdul-Ghani Olabi

Received: 12 January 2024

Revised: 31 January 2024

Accepted: 14 February 2024

Published: 17 February 2024



**Copyright:** © 2024 by the authors. Licensee MDPI, Basel, Switzerland. This article is an open access article distributed under the terms and conditions of the Creative Commons Attribution (CC BY) license (<https://creativecommons.org/licenses/by/4.0/>).

## 1. Introduction

The performance of microbial fuel cells (MFCs) depends on several aspects, including electrode surface area, reactor geometry, conductivity and substrate concentration of the solution, cathode catalyst, and design [1]. Among the many factors affecting the power output of MFCs, the activity of the cathode towards oxygen reduction reaction (ORR) is a key point [2]. Oxygen is the most suitable electron acceptor in MFC cathodes as it is easily available, low cost, non-toxic, and it is more sustainable than the alternatives, including ferricyanide, permanganate, dichromate, and persulfate [3,4]. The ORR is thus a limiting step for electricity production [5], with several issues such as high overpotentials, slow kinetics, and high ohmic resistances [6]. The cathodes are often coupled with proton exchange membranes in a membrane electrode assembly (MEA); hence, the cathode and MEA design are among the most challenging aspects of MFCs. Recently, some researchers have focused on proton exchange membranes to increase the performance of fuel cells, and thin membranes showed the best performances [7]. However, in an MFC, the anodic biofilm must operate strictly under anaerobic conditions, and the crossing of oxygen from the air cathode would result in a dramatic decrease in the performance. Thick membranes are then preferred and used in most studies on MFCs as minimizing the permeation of oxygen is considered more relevant than minimizing the resistance of the membrane [8].

Carbon-based materials are used as cathode supports, such as graphite, carbon cloth, and carbon paper; the main features of these supports are their high specific surface and capability to host catalysts for ORR [9,10]. Precious metals, including Pt and Pd, are highly active catalysts for ORR [11]; however, scarcity, high cost, and the poisoning phenomena

under long-term operations have led to the development of low-cost, precious-metal-free catalysts [9]. Manganese oxide is a valid alternative, and it has previously been proposed as a highly chemically stable, eco-friendly, and cost-effective catalyst for ORR in fuel cells [12,13].

Besides the catalysts for the ORR, several factors affect the MFC performance, including microbes, proton-conducting material, electrode spacing, and system configuration. These design and process parameters can negatively impact the internal resistance of the system, thereby reducing the power output [14,15].

Electrochemical impedance spectroscopy (EIS) is one of the most extensively used steady-state techniques in the characterization of bioelectrochemical systems at a fixed operating potential for the quantitative interpretation of electrochemical features, including polarization resistances and capacitances, fitting the frequency responses with appropriate equivalent circuits (ECs) [16–19]. In an MFC, as described, the maximum power production is a function of the total internal resistance of the system. Quantifying anodic and cathodic impedances will help to minimize the internal resistance of MFCs and to improve the electrical power density.

However, these models may be too simple to interpret the complex phenomena occurring in the system. Previous studies demonstrated that  $R_{\text{int}}$  also contains contributions from the ohmic component in addition to the polarization of the anode and cathode [20], while other authors defined the  $R_{\text{int}}$  as a parameter containing only the contribution of the ohmic component [21], so an EIS characterization of both single electrodes and the whole cell is necessary.

Manohar et al. used the EIS technique to determine the  $R_{\text{int}}$  of an MFC as a function of cell voltage under different anode configurations;  $R_{\text{int}}$  decreased with decreasing potential, with an increase in the maximum power produced by the MFCs. The biofilm formation rate and the initial bacterial growth rate also determine the MFC performance [19]. EIS analyses of the anodic compartment of MFCs studied the limitations of bio-anodes and the relative contributions of diffusion and reaction kinetics [22], as well as the influence of biofilm growth on the resistance to the transfer of charge [23,24]. Understanding the mechanism that limits the performance of the whole system is critical to further improving power production in MFCs.

Based on the analysis of electrode resistances, the cathode has often been identified as the main contributor to cell internal resistance [25] due to the poor solubility of the oxygen and to the mass transfer resistance towards the electrode surface, which is related to the slow kinetics of the ORR; to account for the different processes and limitations, complex equivalent circuits are used to fit the EIS data, which often involve a Warburg element [26].

EIS analysis also provides information on the electrochemical reactions, as well as on the surface of the electrodes, which are critical for electricity generation since the coating layers can influence the polarization resistance [27,28].

The relative humidity is another important factor that may influence the performances of the MEA in MFCs. The evaporation of water depends on the relative humidity, and it may promote membrane dehydration, with a decrease in the performance of the MFC [29]. Humidity levels also influence the oxygen crossover [30]. High values of relative humidity may also lead to pore blocking with inhibition of the ORR through the accumulation of water. MFCs with Nafion, as separators in the MEA, showed the highest power density with a relative humidity of 90% [31].

In this study, MEA were prepared, where Mn oxide electrodeposited onto carbon cloth and subsequently coupled with a mixture of activated carbon (AC) and carbon black (CB) was the catalyst. The as-prepared electrode was then coupled with a proton exchange membrane and used in continuous-flow microbial fuel cells. The performance of the MFCs was assessed; the influence of the catalyst loading on the electricity generation was investigated and compared with the performances of MFCs with carbon and Pt/carbon electrodes. EIS analyses were used to evaluate the contribution of the anode and MEA and

to quantify the kinetics and structural parameters of the cathodes, as well as the effect of air humidity on the ORR [32].

Mn oxide ( $\text{MnO}_x$ ) catalysts have been successfully utilized as cathodes of MFCs for decades [4] because they demonstrate excellent performance and are non-toxic, cost-effective, and environmentally friendly. However, attention has mainly been paid to the intrinsic catalytic activity of the oxide and the modification of the material to improve the poor electrical conductivity of  $\text{MnO}_x$ -based cathodes [33]. The electrodeposition of the catalyst onto the surface of the support has been proposed to increase the conductivity of the electrodes; the deposit was characterized with cyclic voltammetry and electrochemical impedance spectroscopy. To the best of our knowledge, no papers have appeared in the literature with a comprehensive EIS characterization of both the cell and the MEA during the operation of continuous-flow MFCs with electrodeposited Mn oxide as catalyst. The novelty of this work rests on its quantitative interpretation of catalyst loading and operative conditions, including air humidity and external resistance on the kinetics of the ORR and on electricity generation.

## 2. Materials and Methods

### 2.1. Preparation of the MEAs

Three different catalytic layers were tested for the cathodes: (i) manganese oxide/carbon ( $\text{MnX}$ , where X depends on the amount of Mn); (ii) platinum/carbon (Pt/C); and (iii) carbon (AC/CB). All the layers were deposited on a  $5 \text{ cm}^2$  carbon cloth support (CC4, Fuel Cell Earth, Woburn, MA, USA).

$\text{MnX}$  layers were prepared via electrodeposition. Manganese oxide was electrodeposited in a three-electrode beaker cell, with carbon cloth as a working electrode, Pt foil as a counter, and a saturated calomel electrode (SCE, Amel, Italy) as a reference electrode. The deposition was performed at room temperature with a potentiostat–galvanostat (PTG, AUTOLAB PGSTAT 302N with frequency response analyzer, Metrohm, Herisau, Switzerland) in  $0.1 \text{ M Mn}(\text{CH}_3\text{COO})_2$  with  $0.1 \text{ M Na}_2\text{SO}_4$  as a supporting electrolyte [34]. Consecutive cyclic voltammeteries in the potential window between  $0.87$  and  $1.37 \text{ V}$  vs. RHE at a scan rate of  $400 \text{ mVs}^{-1}$  were performed for 10 (Mn10), 20 (Mn20), and 100 (Mn100) min, corresponding to 240, 480, and 2400 cycles, respectively. The amount of manganese oxide electrodeposited was estimated from the voltametric charge with Faraday's law and depends on the number of cycles: values of  $0.039 \text{ mg cm}^{-2}$  (240 cycles);  $0.078 \text{ mg cm}^{-2}$  (480 cycles); and  $0.392 \text{ mg cm}^{-2}$  (2400 cycles) were obtained. After electrodeposition, the prepared electrodes were washed with distilled water and dried in air for 24 h at room temperature. Then, they were analyzed with scanning electron microscopy to verify the presence of the deposit. Figure 1 reports the SEM images of the carbon cloth modified with manganese oxide and clearly shows the uniform distribution of nanoclusters of manganese oxide on the carbon fiber surface; each nanocluster consists of irregular sheets to form a petal-shaped nanostructure of manganese oxide. EDX analysis in Figure 1 confirms the presence of both manganese and oxygen on the carbon-based surface.

To allow for the assembling of the Mn oxide layer with the membrane, the layers were coated via a paint brush technique with an ink composed of 100 mg of activated carbon (AC, Aldrich sieved at 100  $\mu\text{m}$ ), 10 mg of carbon black (CB, Alfa Aesar specific area  $75 \text{ m}^2 \text{ g}^{-1}$  bulk density  $80\text{--}120 \text{ g dm}^{-3}$ ), and 300  $\mu\text{L}$  of Nafion solution (5 wt % in a mixture of lower aliphatic alcohols and water, Merck KGaA, Darmstadt, Germany).

Pt/C layers was prepared via brush technique; the ink was composed of 2.5 mg of commercial Pt catalyst (40 wt % Pt/C, Alfa Aesar), 50 mg of CB, and 300  $\mu\text{L}$  of Nafion solution (5 wt % in a mixture of lower aliphatic-alcohols and water, Sigma Aldrich). The ink was applied to one side of the carbon cloth and dried at room temperature for 24 h. The resulting average loading of Pt was then  $0.2 \text{ mg cm}^{-2}$  [35].

AC/CB electrodes were obtained by brush painting the carbon cloth support with the same ink used for the  $\text{MnX}$  electrodes.

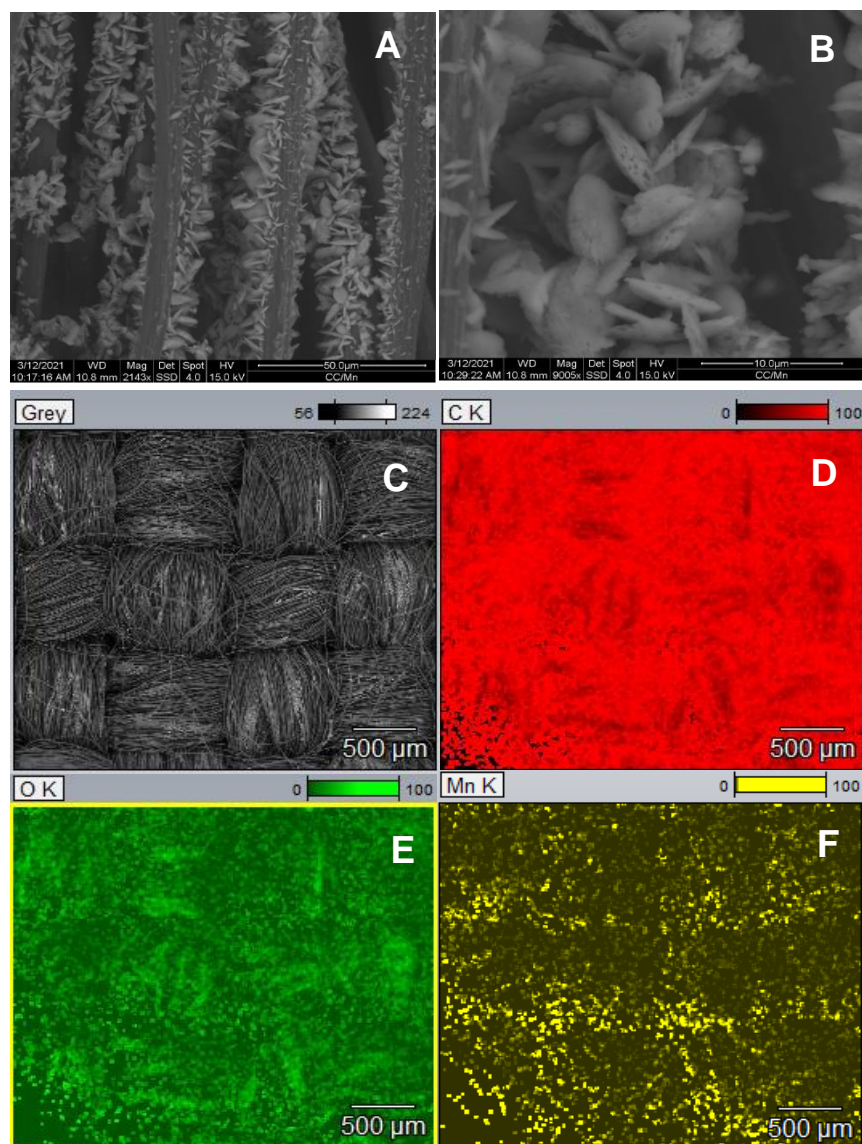


**Figure 1.** SEM images at different magnifications (panels A,B) and energy dispersive X-ray (EDX) mapping analysis of the Mn deposits on carbon cloth (panels C–F).

Finally, MEAs were realized, putting together the synthesized electrodes and a Nafion<sup>®</sup> 115 proton exchange membrane by hot pressing at 105 °C [36]. The MEAs obtained with 10, 20, and 100 min of deposition are denoted as Mn10, Mn20, and Mn100, while those with platinum and with no catalysts were denoted as Pt/C and AC/CB, respectively.

Carbon felt (specific surface area 0.18 m<sup>-2</sup> g<sup>-1</sup>; porosity 95%; Fuel Cell Earth, Woburn, MA USA) was used as the anode. The material was activated as described in ref. [37], and the procedure is detailed in the Supplementary Material.

## 2.2. MFC Set up and Operation

The MFCs used in the experiments are single-cells with air-cathodes and were 3D printed (Form3 printer from Formlabs, Boston, MA, USA, Grey-Pro© resin). The anodic chamber has a cross sectional area of 0.5 cm × 1 cm and a length of 5 cm and is equipped with an inlet and an outlet port (Figure 2A); the felt anode is the same size as the chamber. The anode chamber is open on one side where the cathode was placed. The cell is then closed by a cathodic half-cell with three windows to expose the cathode to the air. The half-cells were kept together with plastic screws and rubber gaskets. The geometric area

of the electrodes ( $5 \text{ cm}^2$ ) was used to calculate the current and power densities in MFC operation, as well as the specific resistances and capacitances in the analyses of impedance spectra with equivalent circuits.

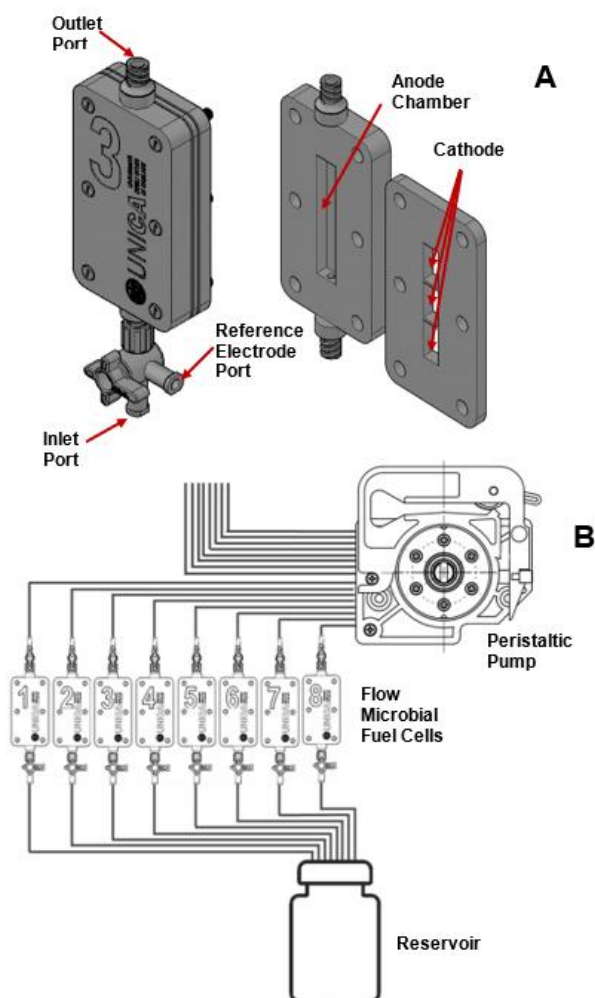


**Figure 2.** Schematic view of the MFC (A) and hydraulic circuit (B).

The electrolyte flowed throughout the cells that operated either in continuous or in batch-recirculated mode. A peristaltic pump (BVP, Ismatec) was used, with eight channels to allow for the operation of up to 8 cells in parallel. The flow rate was  $0.3 \text{ mL min}^{-1}$ . The hydraulic circuit is shown in Figure 2B. In batch-recirculating mode, the electrolyte was pumped from a reservoir throughout the cell and back in a closed loop.

The feeding solution was constituted by the medium and the substrate. The composition of the medium was  $270 \text{ mg L}^{-1} (\text{NH}_4)_2\text{SO}_4$ ;  $60 \text{ mg L}^{-1} \text{MgSO}_4 \cdot 7\text{H}_2\text{O}$ ;  $6 \text{ mg L}^{-1} \text{MnSO}_4 \cdot \text{H}_2\text{O}$ ;  $120 \text{ mg L}^{-1} \text{NaHCO}_3$ ;  $3 \text{ mg L}^{-1} \text{FeCl}_3 \cdot 6\text{H}_2\text{O}$ ; and  $4 \text{ mg L}^{-1} \text{MgCl}_2$ . Sodium acetate  $2 \text{ g L}^{-1}$  was the substrate. The solution was boiled, flowed with nitrogen to remove dissolved oxygen, and cooled. During the runs, the solution was kept at  $30 \text{ }^\circ\text{C}$ . The cells were connected in parallel to  $1 \text{ k}\Omega$  resistor and to a multichannel voltage logger (PicoLog<sup>®</sup>, Pico Technology, St Neots, UK) with Ti wires.

Enrichment of biofilm was performed, feeding the cells with the solution to which 10% of anaerobic sludge was added. The inoculum was provided by a local wastewater treatment plant. The enrichment of the biofilm was carried out with Pt/C cathodes. When the cell voltage was stable (typically  $300 \pm 20 \text{ mV}$ ), Pt/C cathodes were replaced with the electrodes Mn10, Mn20, Mn100, and AC/CB, and feeding solution was pumped into the cells. Each run was carried out in triplicate.

Polarization and power density curves were obtained as follows: the cells were kept under open circuit and then connected to resistors with decreasing resistance, from 10 k $\Omega$  to 10  $\Omega$ , switching the resistors once a steady value of potential was measured; the current ( $I$ ) and power ( $P$ ) were calculated from the voltage ( $E$ ) and the resistance ( $R_{ext}$ ) with Ohm's law ( $E = I \cdot R_{ext}$ ) and Joule's law ( $P = E^2 / R_{ext}$ ); current and power densities were calculated with the geometrical area (5 cm<sup>2</sup>); and the internal resistance  $R_{int}$  was evaluated from the slope of the ohmic region of the polarization curves [25].

### 2.3. EIS Characterization

Electrochemical impedance spectroscopies were used to characterize both MEAs and MFCs.

MFCs were analyzed while operating with the resistance of maximum power. The cells were characterized in a two-electrode setup, where the bioanode was connected to the working electrode port of the PTG and the cathode was connected to the counter and reference ports. The response of the bioanodes was also obtained via separate experiments with a three-electrode set up; the bioanode was the working electrode and the cathode the counter electrode, while a saturated calomel electrode (SCE) was inserted in the relevant port of the cell (see Figure 2) and used as the reference electrode.

A different setup was used to characterize the MEAs, with the cathode as the working electrode and the carbon felt bioanode replaced with a Pt foil connected to both the counter and the reference electrode ports. EIS data were obtained under the potentiostatic mode, as cell voltages were superimposed with values that were obtained from LSV (data not shown) to acquire the same current densities of the MEAs when operating as air-breathing cathodes in the MFCs.

All the EIS data were obtained in a frequency range of 100 kHz–0.1 Hz. The data were verified with Kramers–Kronig transforms.

## 3. Results and Discussion

A preliminary assessment of the optimal catalyst loading was undertaken with steady-state polarization curves of the MEA in microbial fuel cells; the Pt/C cathodes used for the enrichment of biofilm were replaced with the manganese-oxide-based ones, and the cells then operated under continuous-flow conditions with the medium solution and 2 g L<sup>-1</sup> of acetate as feed. In Figure 3, the power curves and the polarization curves obtained with three Mn-based cathodes are compared with those obtained with AC/CB and Pt/C cathodes. As shown, the maximum power density (MPD) of the Mn-based cathodes is about twice that obtained with bare AC/CB; the MPD of Mn10 is about 2.2-times higher than that of AC/CB electrode and about 20% higher than that of the Pt/C electrode, while higher loadings lead to values of power densities similar to those obtained with Pt/C. The internal resistances of the cells with MnO<sub>x</sub> cathodes were evaluated from the slope of the linear region of the polarization curves (see Supplementary Material, Figure S1); values from 380 to 410  $\Omega$  were obtained, with no appreciable differences among the three samples. OCP values of 540  $\pm$  10 mV were obtained with Mn20 and Mn100, while 565  $\pm$  10 mV was obtained with Mn10. Similar results can be found in the literature, where manganese-oxide-based electrodes were used as catalysts in MFCs. Mn oxides electrodeposited onto the surface of the electrodes showed performances comparable with Pt [35], while lower efficiencies were obtained when powders of MnO<sub>x</sub> mixed with graphite were used. Moreover, in this work, it was found that a low catalyst loading is sufficient to support the operative current densities of MFCs [38] as higher values reduce the performance [34].

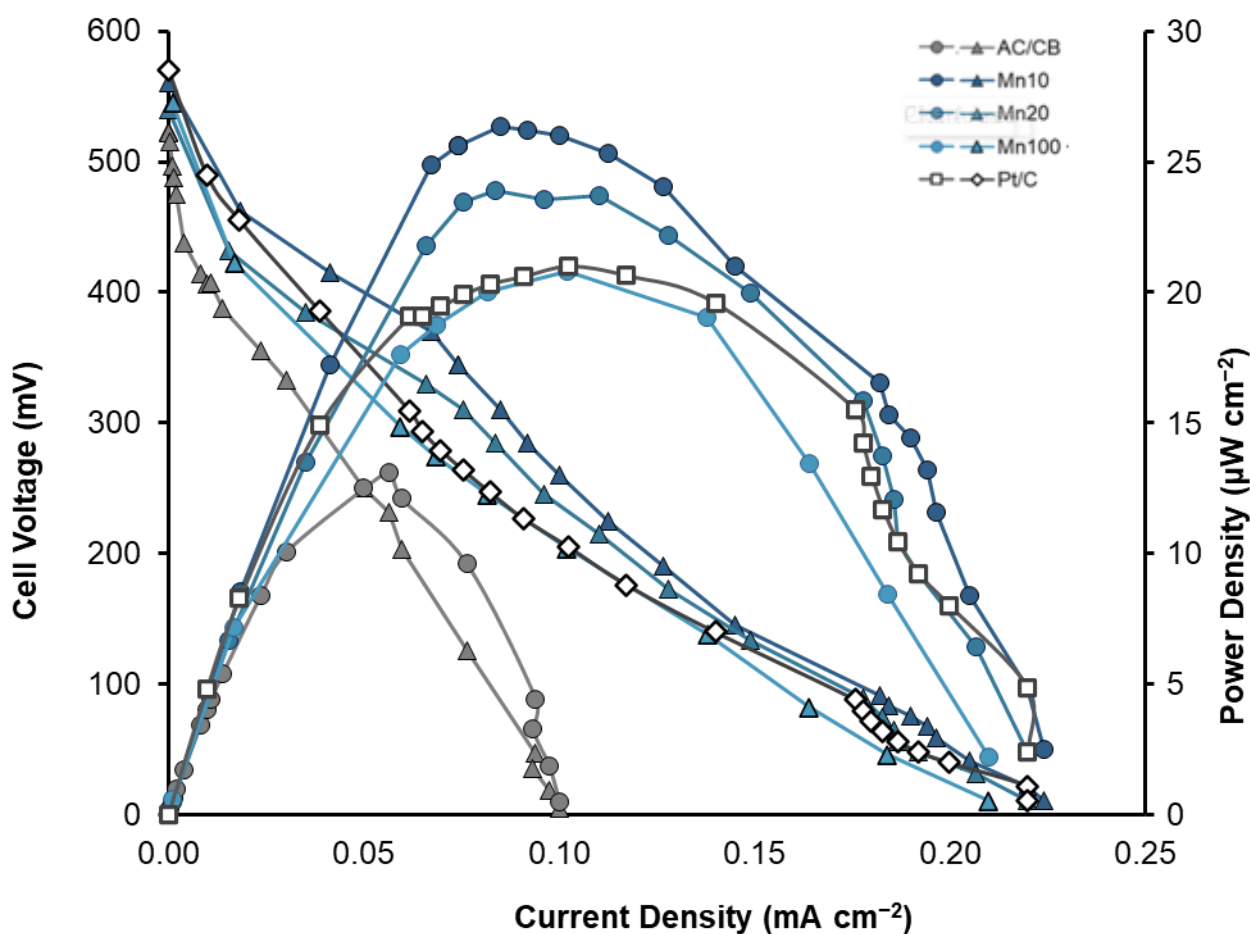


**Figure 3.** Polarization curves and power output of the MFCs with different cathodes.

EIS characterization of the MEA was then carried out to assess the impact of catalyst loading and operative conditions on the performance of the system. Moreover, since it was proven that air humidity plays a crucial role, the characterizations have been performed by equilibrating the cathode with either dry or saturated air [31].

Figure 4 shows the Nyquist plots obtained under different conditions with Mn10; as a comparison, the relevant data of AC/CB are also shown. The corresponding Bode plots are reported in Figures S2 and S3.

As shown, the differences in the Nyquist plots are mainly present in the real part of the impedances, with the largest variation in the curves denoting the applied potential observed with data obtained in dry air. The curves shift to the right with the cathodic potential as  $Z'$  increases and  $Z''$  decreases. The curves obtained in saturated air are left-shifted as the intrinsic resistances of the electrodes decrease with the humidity, as can also be observed in the magnitude of the Bode plots.

The effects were then quantified with equivalent circuits. Before being analyzed, data were validated with a Kramers–Koenig test; the residuals obtained were less than 1% for the whole frequency range, with chi-squared values lower than  $9 \times 10^{-4}$  (all the chi-squared values are reported in Table S1a–d). These values were assumed as a confirmation of Kramers–Kronig validity, and the data were further analyzed with the equivalent circuit in Figure 4.

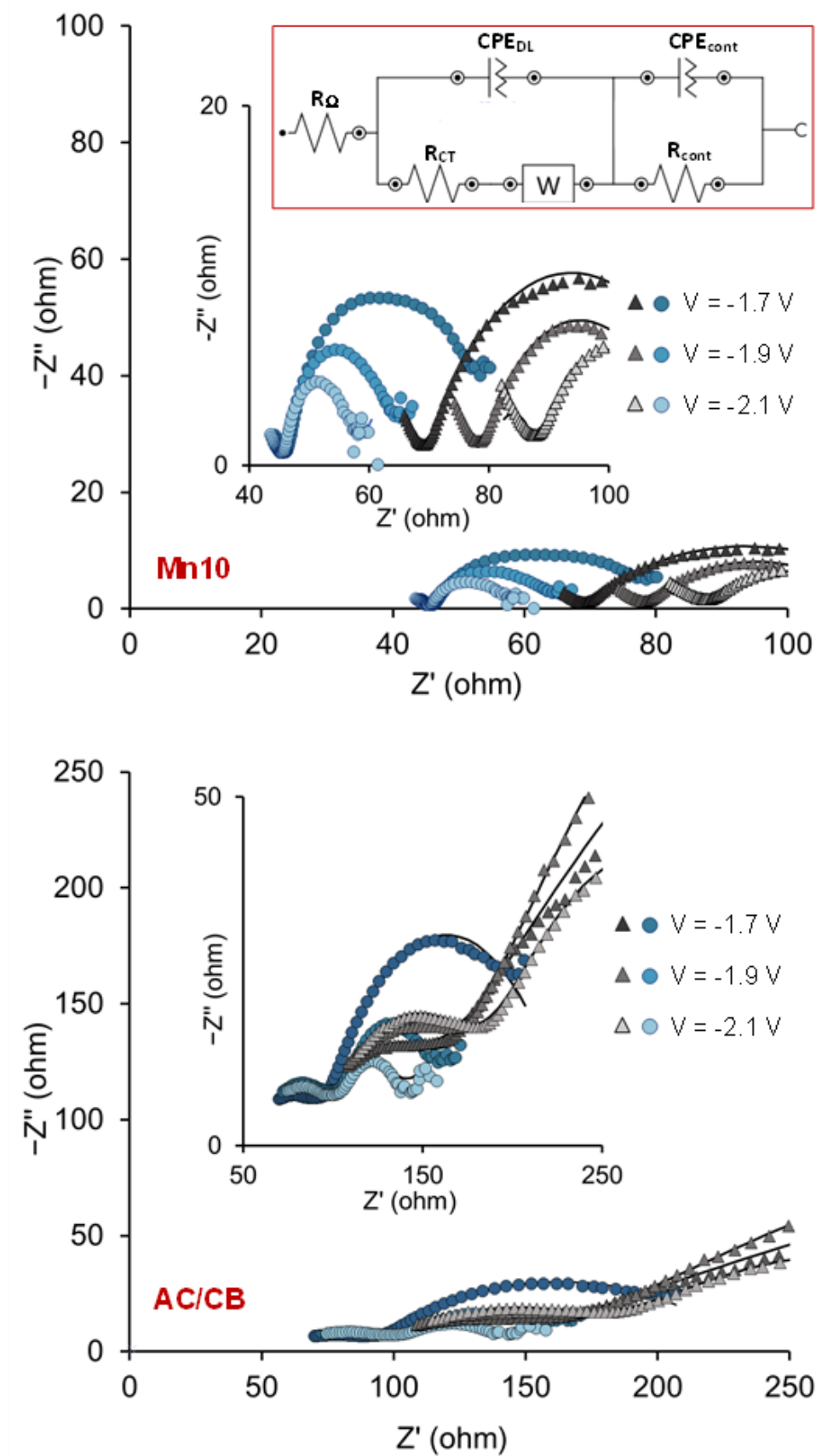


**Figure 4.** Nyquist plots obtained from EIS experiments with dry air (black symbols) and saturated air (blue symbols). The lines have been calculated with the equivalent circuit in the inset.

The circuit includes a resistor ( $R_{\Omega}$ ) to quantify the effects of ohmic resistances of the electrolyte and membrane, two resistive-capacitive elements, and a Warburg element. Constant phase elements (Admittance =  $Y_0(j\omega)^n$ ) were used rather than pure capacities to account for inhomogeneous conditions such as electrode roughness, coating, and the distribution of reaction sites [39]. Table S1 resumes the circuit parameters along with the chi-squared values of the fits, which were always lower than  $4 \times 10^{-4}$ .

Table 1 reports the equivalent capacitance values ( $C_{eq} = (RY_0)^{1/n}/R$ ) calculated from the parameters of the CPEs at high and low frequencies from data obtained with dry air. As a comparison, the values from EIS analyses with Pt/C EIS data are also reported.

**Table 1.** Equivalent capacitances calculated in different frequency ranges for Mn10, Pt, and AC/CB cathodes in dry conditions.

	$C_{DL}$ (F/cm <sup>2</sup> )			$C_{cont}$ (F/cm <sup>2</sup> )		
	Applied Cell Voltage (V)			Applied Cell Voltage (V)		
	1.7	1.9	2.1	1.7	1.9	2.1
AC/CB	$2.50 \times 10^{-3}$	$6.02 \times 10^{-4}$	$1.03 \times 10^{-4}$	$2.59 \times 10^{-8}$	$4.33 \times 10^{-8}$	$4.08 \times 10^{-8}$
Mn10	$1.60 \times 10^{-4}$	$9.37 \times 10^{-5}$	$9.43 \times 10^{-5}$	$5.43 \times 10^{-8}$	$2.92 \times 10^{-8}$	$8.83 \times 10^{-8}$
Pt/C	$7.20 \times 10^{-5}$	$5.43 \times 10^{-5}$	$4.87 \times 10^{-5}$	$1.91 \times 10^{-8}$	$1.19 \times 10^{-8}$	$5.28 \times 10^{-9}$

The elements with capacitances evaluated at high frequencies were attributed to the contact resistance at the interface between the cathode and the current collector ( $R_{cont}$ ,  $C_{cont}$ ) [40,41] as the values of capacitance obtained are lower than the typical double-layer capacitance, which is in the order of  $\approx 10^{-5}$  F/cm<sup>2</sup>. The resistor and capacitor of the second element in the equivalent circuit can be related to the double-layer capacitance ( $C_{DL}$ ) of the active surface and to the charge transfer resistance ( $R_{CT}$ ).

As shown, Pt/C shows a value of  $C_{DL}$  lower than that obtained with AC/CB, while comparable values of  $C_{DL}$  are observed with Mn10 and AC/CB due to the different techniques of preparation of the cathode.

Figure 5 reports the resistances derived from the EIS modeling under dry conditions with different applied potentials.

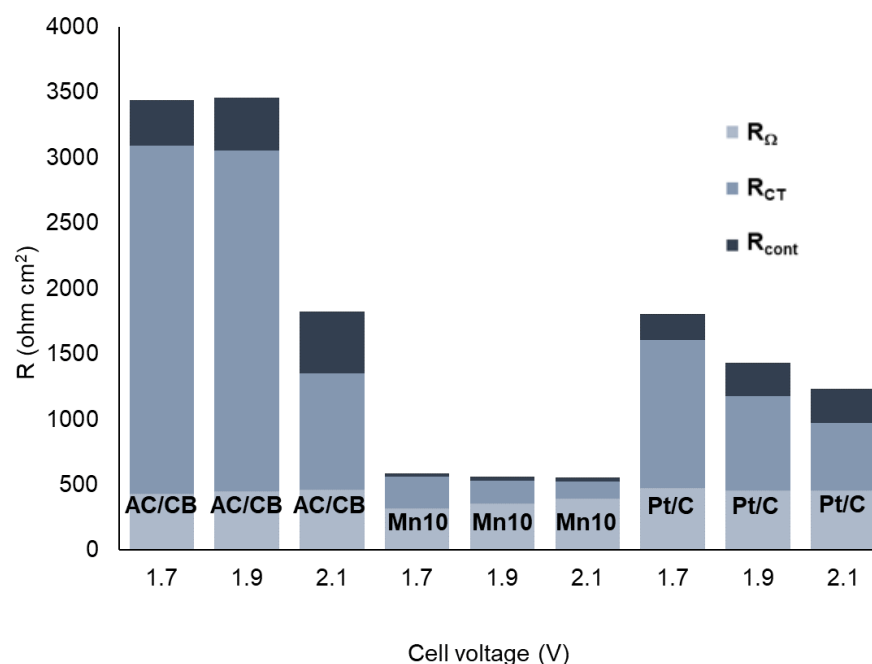
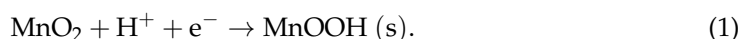


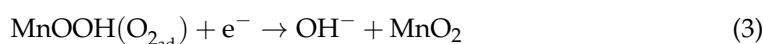
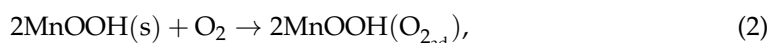
**Figure 5.** Values of resistances derived from EIS analysis of the different cathodes in dry air.

The values of the contact resistances of AC/CB and Pt/C are similar and scarcely influenced by the applied potential, while the resistances at the low frequencies, correlated to the charge transfer processes ( $R_{CT}$ ), are lower for Pt/C. Moreover, Mn10 shows the lowest resistances in all the frequency ranges, which may result from the higher number of active sites exposed to the solution ( $R_{CT}$ ) and the better contact of the modified cathodes. The values of  $R_{CT}$  agree with the relevant  $C_{DL}$ , as a low charge transfer velocity results in a high charge density in the diffusion layer [42].

The reduction of the oxygen at  $MnO_2$  occurs with reduction of  $MnO_2$  to  $MnOOH$ :



This is followed by the adsorption of  $O_2$  and reduction to the  $MnO_2$  phase (Equations (2) and (3)):



The higher the rate of the first step, the lower the number of ions adsorbed on the electrode surface. This may explain the  $C_{DL}$  decrease in Table 1. The structural modification is also assessed vis the right shift of the Nyquist plot with the lowering of potential, which may be related to the lower conductivity of the  $MnOOH$  phase (Equation (1)) [43,44].

The effect of the surface modification can be observed in Figure 6, which shows the EIS data under dry conditions with the cell voltage set at 1.7 V obtained with the as-prepared sample (blue curve) and with a sample polarized with three cycles at 1.7 V, 1.9 V, and 2.1 V. A new semicircle appears, and a further RC element was necessary to fit the data (the circuit parameters are resumed in Table S1b). The new feature in the Nyquist plot can be attributed to the formation of the reversible film already observed by other authors in nanostructured anode materials such as  $Co_3O_4$ ,  $Fe_2O_3$ , and  $MnO$  [45]. Comparing the values of equivalent capacitances, the  $C_{DL}$  did not show significant variation, while the third element, with a capacitance of  $1.78 \times 10^{-3} \text{ F/cm}^2$ , quantifies the pseudo capacitive contribution due to the higher reactivity of the external surface. The surface modification also increases the overall resistance of the process by about 25% (Table S1).

The effect of the humidity was assessed via EIS analyses with saturated air. Table 2 resumes the equivalent capacitances calculated from EIS parameters. The full set of circuit parameters is reported in Table S1a–d.

**Table 2.** Equivalent capacitances calculated in different ranges of frequencies for Mn10, Pt, and AC/CB cathodes in saturated conditions.

	$C_{DL} \text{ (F/cm}^2\text{)}$			$C_{CONT} \text{ (F/cm}^2\text{)}$		
	Applied Cell Voltage (V)			Applied Cell Voltage (V)		
	1.7	1.9	2.1	1.7	1.9	2.1
AC/CB	$1.45 \times 10^{-4}$	$7.26 \times 10^{-5}$	$4.42 \times 10^{-5}$	$2.95 \times 10^{-8}$	$2.89 \times 10^{-8}$	$1.86 \times 10^{-8}$
Mn10	$1.87 \times 10^{-4}$	$3.82 \times 10^{-5}$	$4.16 \times 10^{-5}$	$1.16 \times 10^{-8}$	$3.23 \times 10^{-7}$	$1.89 \times 10^{-7}$
Pt/C	$1.58 \times 10^{-4}$	$8.70 \times 10^{-5}$	$8.56 \times 10^{-5}$	$2.38 \times 10^{-8}$	$2.57 \times 10^{-8}$	$2.57 \times 10^{-8}$

The resistances evaluated from the EIS analyses are reported in Figure 7. In all the frequency ranges, the values of the resistances are lower in saturated than in dry conditions due to the hydration of the surface [31]. Moreover, Mn10 shows lower resistances with respect to AC/CB and Pt/C.

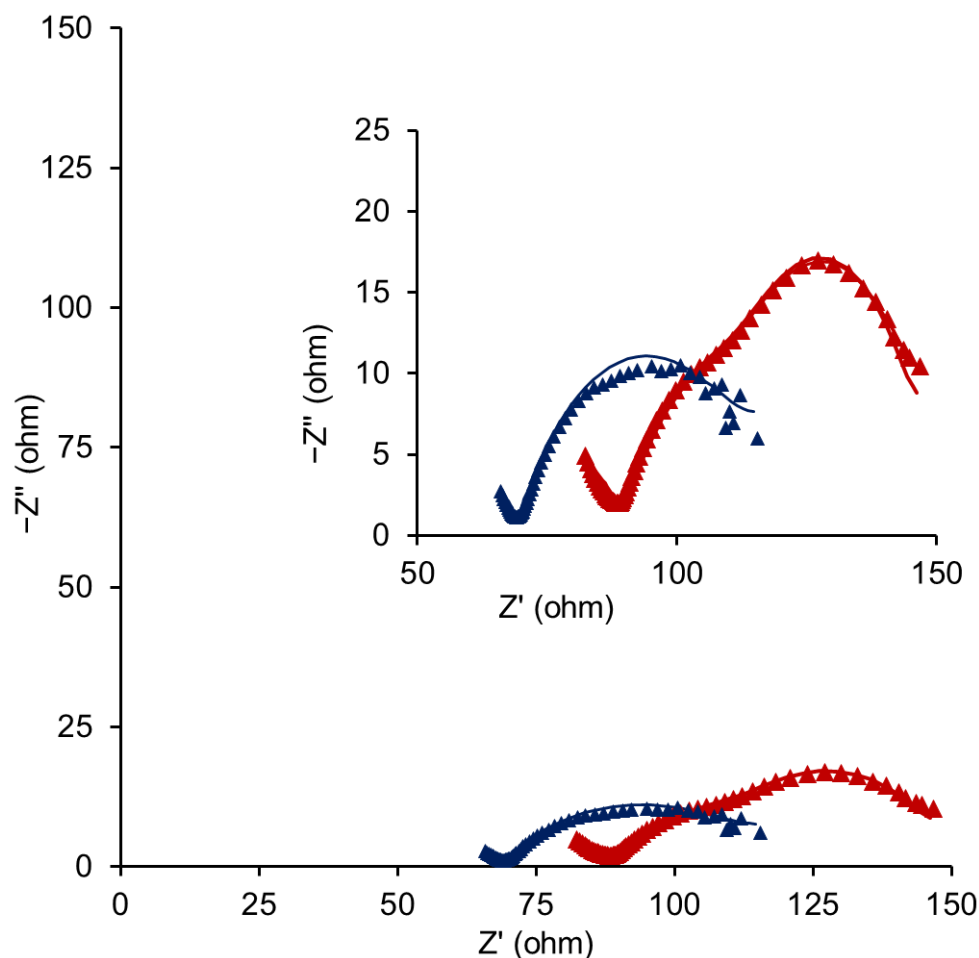


**Figure 6.** Nyquist plots of Mn10 samples (main plot isometric axes; inset magnified axes) obtained via EIS at a cell voltage of 1.7 V in dry air with the as-prepared electrodes (blue) and after three cycles of polarization at 1.7 V, 1.9 V, and 2.1 V (red). Blue lines were calculated with the equivalent circuit in Figure 4; red lines were calculated with the same circuit. A further RQ element was also added.

The values of charge transfer resistances of Pt/C and AC/CB are quite similar, while Mn10 shows lower  $R_{CT}$ , thus indicating higher catalytic activity. This behavior can be explained considering the different characteristics of the electrodes; the Mn oxides are electro-deposited onto the surface of the carbon cloth in the Mn10 electrodes, as AC/CB has no catalyst, and the Pt particles in Pt/C are dispersed in the carbon matrix. Electrodeposition allows for a better distribution of the catalysts onto the support; thus, a higher amount of active site is available for the reaction. Moreover, as observed from SEM analyses, the deposit of Mn oxide is grown on the fibers of carbon cloth, resulting in a lower electric resistance as shown by the values of  $R_Q$  in Figure 7.

To investigate the occurrence of the structural modifications observed in dry air after polarization, EIS data at 1.7 V of the as-prepared sample were compared with those of a sample after polarization. In saturated air, no appreciable differences were observed in the Nyquist plots before and after the polarization, and so too in the values of the resistances), indicating that the steps in Equations (2) and (3) are faster in saturated air than in dry air, and the catalytic  $MnO_2$  sites have been restored.

EIS analysis of the MFCs and of the anode in operation were then carried out to quantify the effect of the cathode/membrane and cathode/catalyst assembly on the performance of the system. Mn10 cathodes were used in the analyses, and the EIS data were obtained for the cell operating with the external resistance of maximum power output. Figure 8 shows the relevant Nyquist plots.

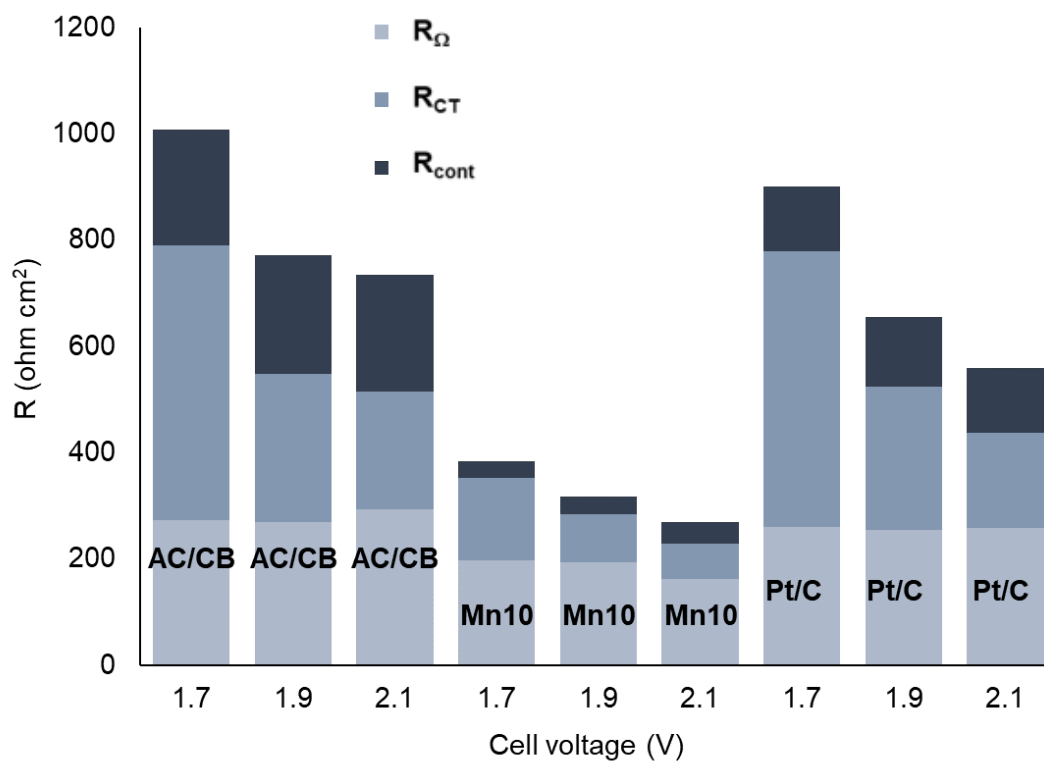


Figure 7. Values of resistances derived from EIS analysis of the different cathodes in saturated air.

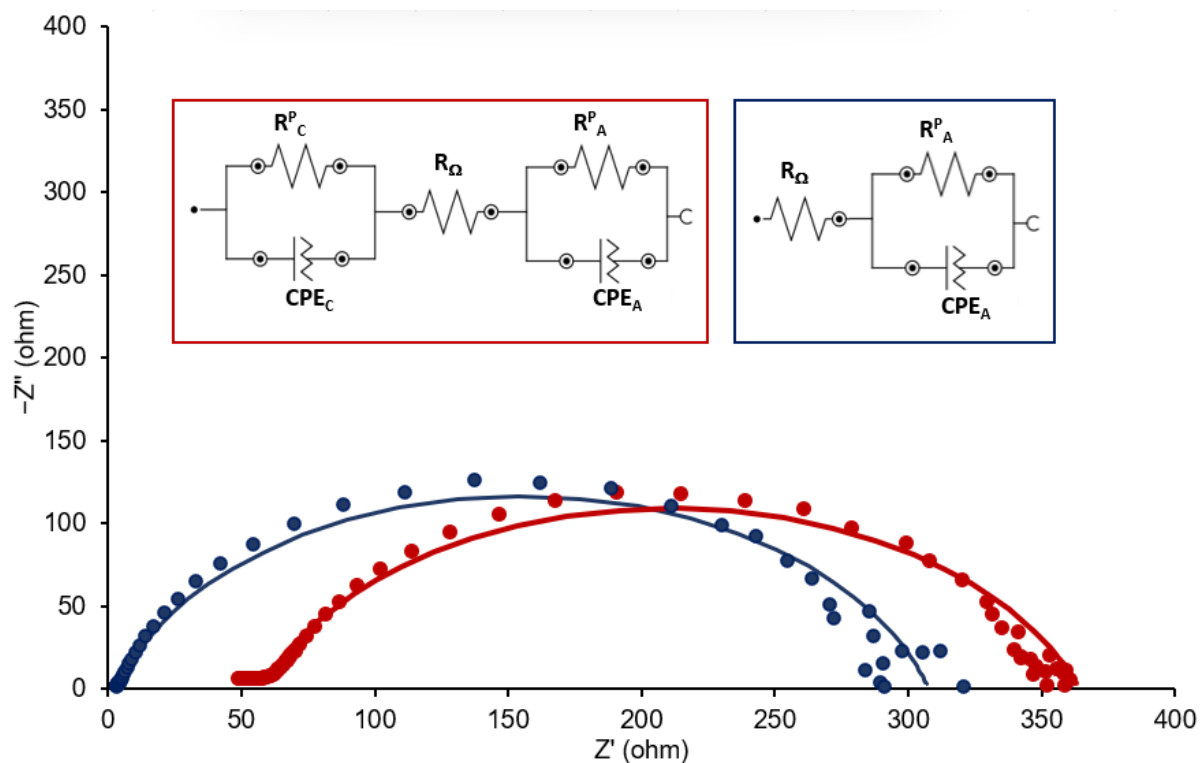


Figure 8. Nyquist plot of the MFC (red) and the anode (blue) performed during operation with the external resistance of maximum power. Lines are calculated with the equivalent circuits in the insets.

A well-defined semicircle is obtained as the contribution of the polarization resistance (the diameter of the circles in Figure 8) to the impedance of MFCs is dominant. Figure also shows the equivalent circuits used to quantify anode (A), cathode (C), and ohmic

( $\Omega$ ) resistance (circuit parameters in Table S2). As the impedance of the MFC depends on the anode, cathode, and other components, the internal resistance ( $R_{\text{int}}$ ) could be defined as [19]

$$R_{\text{int}} = R^P_{\text{A}} + R^P_{\text{C}} + R_{\Omega}, \quad (4)$$

where  $R^P_{\text{A}}$  and  $R^P_{\text{C}}$  are the polarization resistances of the anode and cathode, respectively, and  $R_{\Omega}$  is the result of the ohmic resistances of electrodes, cell, and membrane. The relevant contribution of the different parts depends on the design and operative conditions; either the cathode [46,47] or the bioanode [48] were found to be limiting factors of the polarization resistance.

The values of  $R^P_{\text{A}}$  and  $R^P_{\text{C}}$  of 304 ohm and 59.2 ohm, respectively, were obtained while  $R_{\Omega}$  was 3.35 ohm. The polarization resistance of the anode is then clearly prevalent, as has been found in other studies [19].

In a previous work, the effect of design parameters for miniature cells with carbon felt anodes was assessed; based on the results obtained, the arrangement of the electrodes used in this work minimizes the resistance of the cell as the feed is pumped throughout the anode with no interelectrode gap [49].

The polarization resistance of the cathodes in MFC may represent a major contribution to the overall resistance of the cell. Lapage et al. found that the resistive contribution for the overall cell is mainly brought about by the cathode compartment using open-pore vitreous carbon foam as both anode and cathode [26], while Tremouli et al. measured the comparable contributions of both anode and cathode in an MFC with plain carbon paper as the anode and carbon cloth with  $0.5 \text{ mg cm}^{-2}$  of Pt as the cathode [50].

With the experimental setup used in this work, the cathode, however, contributes to about 15%, confirming the relevance of the MEA to the overall resistance, as well as the importance of good MEA design.

#### 4. Conclusions

Membrane electrode assembly was prepared by putting together a proton exchange membrane and Mn-oxide-based electrodes, which were obtained through electrodeposition onto the surface of carbon cloth. Membrane electrode assembly with different  $\text{MnO}_2$  loading has been tested and compared with either carbon or carbon/Pt electrodes in MFC operation via polarization experiments and electrochemical impedance spectroscopies.

MFCs with electrodeposited Mn oxides showed higher power densities than MFCs with carbon or carbon/Pt electrodes in MFC operation. Values of maximum power density (MPD) of  $280 \text{ mW m}^{-2}$  were obtained with Mn oxide as a catalyst, while the cells with Pt/C cathodes showed an MPD of  $210 \text{ mW m}^{-2}$ . The design of the cell and operative conditions, including feed and biofilm composition, strongly influenced the MPD; so, values can be found from  $1.5 \text{ mW m}^{-2}$  to  $1500 \text{ mW m}^{-2}$  with different cathodes and depending on cell design and operation [51]. A direct comparison with values from the literature should be very carefully made. Under conditions similar to this work, an MPD of about  $320 \text{ mW m}^{-2}$  was obtained with Pt/C electrodes [49]. As MPDs of hundreds of  $\text{mW m}^{-2}$  are among the best values for flow MFCs, the performance of the Mn oxide electrodes here tested is satisfactory.

EIS of the membrane cathode assembly was then used to identify the working mechanism of the oxygen reduction reaction. Structural modifications induced by the reduction of the active sites during ORR were investigated with both dry and water-saturated air.

The humidity in the air was found to be the most influential factor for the performance of the Mn-oxide-based cathodes as in dry air, the resistances of the MEA measured via EIS were threefold those obtained in water-saturated air.

The effect of humidity is strongly related to the mechanism of OER on  $\text{MnO}_2$  cathodes, particularly to the reversibility of the reduction of  $\text{Mn}^{4+}$  to  $\text{Mn}^{3+}$ . With dry air and the current density typical of MFCs, the system appears to be unable to restore the  $\text{MnO}_2$ , and the related adsorption of  $\text{O}_2$  is activated, along with the simultaneous consumption of  $\text{Mn}^{4+}$ . Reactivation of the system could be improved by increasing the local humidity, as well as

by improving humidification as in saturated air conditions, the structural transformation is fully reversible.

**Supplementary Materials:** The following supporting information can be downloaded at: <https://www.mdpi.com/article/10.3390/en17040943/s1>, Figure S1: Slopes of the linear region of the polarization curves; Figure S2: Bode plots obtained from EIS experiments with Mn10 electrodes; Figure S3: Bode plots obtained from EIS experiments with AC/CB electrodes; Table S1: (a–d): Parameters of the equivalent circuits used to characterize the cathodes.

**Author Contributions:** Conceptualization, A.V., L.M. and M.M.; formal analysis, L.M. and M.M.; investigation, L.M.; data curation, L.M. and A.V.; writing—original draft preparation, L.M.; writing—review and editing A.V. and M.M. All authors have read and agreed to the published version of the manuscript.

**Funding:** This research was funded by the Italian minister of University and Research within the Next-Generation EU framework (project code MUR: PE0000005 CUP: F53C22000730002).

**Data Availability Statement:** Data will be available on demand.

**Acknowledgments:** This paper is part of the research project RETURN (multi-risk science for resilient communities under a changing climate), funded within the Next-Generation EU framework (project code MUR: PE0000005 CUP: F53C22000730002).

**Conflicts of Interest:** The authors declare no conflict of interest.

## References

1. Naha, A.; Debroy, R.; Sharma, D.; Shah, M.P.; Nath, S. Microbial Fuel Cell: A State-of-the-Art and Revolutionizing Technology for Efficient Energy Recovery. *Clean. Circ. Bioecon.* **2023**, *5*, 100050. [[CrossRef](#)]
2. Chen, J.; Yang, J.; Wang, R.; Yang, Y.; Liu, Y. Design and Research Progress of Nano Materials in Cathode Catalysts of Microbial Fuel Cells: A Review. *Int. J. Hydrogen Energy* **2022**, *47*, 18098–18108. [[CrossRef](#)]
3. Ucar, D.; Zhang, Y.; Angelidaki, I. An Overview of Electron Acceptors in Microbial Fuel Cells. *Front. Microbiol.* **2017**, *8*, 248548. [[CrossRef](#)] [[PubMed](#)]
4. Ben Liew, K.; Daud, W.R.W.; Ghasemi, M.; Leong, J.X.; Su Lim, S.; Ismail, M. Non-Pt Catalyst as Oxygen Reduction Reaction in Microbial Fuel Cells: A Review. *Int. J. Hydrogen Energy* **2014**, *39*, 4870–4883. [[CrossRef](#)]
5. Elangovan, K.; Saravanan, P.; Campos, C.H.; Sanhueza-Gómez, F.; Khan, M.M.R.; Chin, S.Y.; Krishnan, S.; Viswanathan Mangalaraja, R. Outline of Microbial Fuel Cells Technology and Their Significant Developments, Challenges, and Prospects of Oxygen Reduction Electrocatalysts. *Front. Chem. Eng.* **2023**, *5*, 1228510. [[CrossRef](#)]
6. Ramya, M.; Senthil Kumar, P. A Review on Recent Advancements in Bioenergy Production Using Microbial Fuel Cells. *Chemosphere* **2022**, *288*, 132512. [[CrossRef](#)] [[PubMed](#)]
7. Shang, Z.; Wycisk, R.; Pintauro, P. Electrospun Composite Proton-Exchange and Anion-Exchange Membranes for Fuel Cells. *Energies* **2021**, *14*, 6709. [[CrossRef](#)]
8. Banerjee, A.; Calay, R.K.; Eregno, F.E. Role and Important Properties of a Membrane with Its Recent Advancement in a Microbial Fuel Cell. *Energies* **2022**, *15*, 444. [[CrossRef](#)]
9. Rodríguez, J.; Mais, L.; Campana, R.; Piroddi, L.; Mascia, M.; Gurauskis, J.; Vacca, A.; Palmas, S. Comprehensive Characterization of a Cost-Effective Microbial Fuel Cell with Pt-Free Catalyst Cathode and Slip-Casted Ceramic Membrane. *Int. J. Hydrogen Energy* **2021**, *46*, 26205–26223. [[CrossRef](#)]
10. Wilberforce, T.; Abdelkareem, M.A.; Elsaid, K.; Olabi, A.G.; Sayed, E.T. Role of Carbon-Based Nanomaterials in Improving the Performance of Microbial Fuel Cells. *Energy* **2022**, *240*, 122478. [[CrossRef](#)]
11. Quan, X.; Mei, Y.; Xu, H.; Sun, B.; Zhang, X. Optimization of Pt-Pd Alloy Catalyst and Supporting Materials for Oxygen Reduction in Air-Cathode Microbial Fuel Cells. *Electrochim. Acta* **2015**, *165*, 72–77. [[CrossRef](#)]
12. Osgood, H.; Devaguptapu, S.V.; Xu, H.; Cho, J.; Wu, G. Transition Metal (Fe, Co, Ni, and Mn) Oxides for Oxygen Reduction and Evolution Bifunctional Catalysts in Alkaline Media. *Nano Today* **2016**, *11*, 601–625. [[CrossRef](#)]
13. Aysla Costa De Oliveira, M.; D'Epifanio, A.; Ohnuki, H.; Mecheri, B. Platinum Group Metal-Free Catalysts for Oxygen Reduction Reaction: Applications in Microbial Fuel Cells. *Catalysts* **2020**, *10*, 475. [[CrossRef](#)]
14. Neethu, B.; Khandelwal, A.; Ghangrekar, M.M.; Ihjas, K.; Swaminathan, J. Microbial Fuel Cells—Challenges for Commercialization and How They Can Be Addressed. In *Scaling Up of Microbial Electrochemical Systems*; Elsevier: Amsterdam, The Netherlands, 2022; pp. 393–418. [[CrossRef](#)]
15. Jayapriya, J.; Gummadi, S.N. Scaling up and Applications of Microbial Fuel Cells. In *Scaling Up of Microbial Electrochemical Systems: From Reality to Scalability*; Elsevier: Amsterdam, The Netherlands, 2022; pp. 309–338. [[CrossRef](#)]
16. Wang, H.; Long, X.; Sun, Y.; Wang, D.; Wang, Z.; Meng, H.; Jiang, C.; Dong, W.; Lu, N. Electrochemical Impedance Spectroscopy Applied to Microbial Fuel Cells: A Review. *Front. Microbiol.* **2022**, *13*, 973501. [[CrossRef](#)] [[PubMed](#)]

17. Kim, B.; Chang, I.S.; Dinsdale, R.M.; Guwy, A.J. Accurate Measurement of Internal Resistance in Microbial Fuel Cells by Improved Scanning Electrochemical Impedance Spectroscopy. *Electrochim. Acta* **2021**, *366*, 137388. [[CrossRef](#)]
18. Antonopoulou, G.; Bampos, G.; Ntaikou, I.; Alexandropoulou, M.; Dailianis, S.; Bebelis, S.; Lyberatos, G. The Biochemical and Electrochemical Characteristics of a Microbial Fuel Cell Used to Produce Electricity from Olive Mill Wastewater. *Energy* **2023**, *282*, 128804. [[CrossRef](#)]
19. Manohar, A.K.; Mansfeld, F. The Internal Resistance of a Microbial Fuel Cell and Its Dependence on Cell Design and Operating Conditions. *Electrochim. Acta* **2009**, *54*, 1664–1670. [[CrossRef](#)]
20. Bazina, N.; Ahmed, T.G.; Almdaaf, M.; Jibia, S.; Sarker, M. Power Generation from Wastewater Using Microbial Fuel Cells: A Review. *J. Biotechnol.* **2023**, *374*, 17–30. [[CrossRef](#)] [[PubMed](#)]
21. Aelterman, P.; Rabaey, K.; Pham, H.T.; Boon, N.; Verstraete, W. Continuous Electricity Generation at High Voltages and Currents Using Stacked Microbial Fuel Cells. *Environ. Sci. Technol.* **2006**, *40*, 3388–3394. [[CrossRef](#)] [[PubMed](#)]
22. Rossi, R.; Hall, D.M.; Wang, X.; Regan, J.M.; Logan, B.E. Quantifying the Factors Limiting Performance and Rates in Microbial Fuel Cells Using the Electrode Potential Slope Analysis Combined with Electrical Impedance Spectroscopy. *Electrochim. Acta* **2020**, *348*, 136330. [[CrossRef](#)]
23. Sonawane, J.M.; Mahadevan, R.; Pandey, A.; Greener, J. Recent Progress in Microbial Fuel Cells Using Substrates from Diverse Sources. *Heliyon* **2022**, *8*, e12353. [[CrossRef](#)] [[PubMed](#)]
24. Ortiz-Medina, J.F.; Call, D.F. Electrochemical and Microbiological Characterization of Bioanode Communities Exhibiting Variable Levels of Startup Activity. *Front. Energy Res.* **2019**, *7*, 478969. [[CrossRef](#)]
25. Rossi, R.; Cario, B.P.; Santoro, C.; Yang, W.; Saikaly, P.E.; Logan, B.E. Evaluation of Electrode and Solution Area-Based Resistances Enables Quantitative Comparisons of Factors Impacting Microbial Fuel Cell Performance. *Environ. Sci. Technol.* **2019**, *53*, 3977–3986. [[CrossRef](#)]
26. Lepage, G.; Albernaz, F.O.; Perrier, G.; Merlin, G. Characterization of a Microbial Fuel Cell with Reticulated Carbon Foam Electrodes. *Bioresour. Technol.* **2012**, *124*, 199–207. [[CrossRef](#)] [[PubMed](#)]
27. Liu, Y.; Guo, S.; Wang, J.; Li, C. Fundamental Development and Research of Cathodic Compartment in Microbial Fuel Cells: A Review. *J. Environ. Chem. Eng.* **2022**, *10*, 107918. [[CrossRef](#)]
28. Sekar, N.; Ramasamy, R.P. Electrochemical Impedance Spectroscopy for Microbial Fuel Cell Characterization. *J. Microb. Biochem. Technol.* **2013**, *5*, 1948–5948. [[CrossRef](#)]
29. Lee, M.; Kakarla, R.; Min, B. Performance of an Air-Cathode Microbial Fuel Cell under Varied Relative Humidity Conditions in the Cathode Chamber. *Bioprocess Biosyst. Eng.* **2019**, *42*, 1247–1254. [[CrossRef](#)]
30. Kakarla, R.; Kim, J.R.; Jeon, B.H.; Min, B. Enhanced Performance of an Air–Cathode Microbial Fuel Cell with Oxygen Supply from an Externally Connected Algal Bioreactor. *Bioresour. Technol.* **2015**, *195*, 210–216. [[CrossRef](#)]
31. Lee, M.; Kondaveeti, S.; Jeon, T.; Kim, I.; Min, B. Influence of Humidity on Performance of Single Chamber Air-Cathode Microbial Fuel Cells with Different Separators. *Processes* **2020**, *8*, 861. [[CrossRef](#)]
32. Vacca, A.; Palmas, S.; Mascia, M.; Piras, L.; Mais, L. Continuous-flow microbial fuel cells with electrodeposited MnOx as catalyst for the oxygen reduction reaction. In Proceedings of the 4th Edition of the E3 Mediterranean Symposium: Electrochemistry for Environment and Energy (E3MS), Orvieto, Italy, 15–17 September 2022.
33. Qiu, S.; Guo, Z.; Naz, F.; Yang, Z.; Yu, C. An Overview in the Development of Cathode Materials for the Improvement in Power Generation of Microbial Fuel Cells. *Bioelectrochemistry* **2021**, *141*, 107834. [[CrossRef](#)]
34. Liu, X.W.; Sun, X.F.; Huang, Y.X.; Sheng, G.P.; Zhou, K.; Zeng, R.J.; Dong, F.; Wang, S.G.; Xu, A.W.; Tong, Z.H. Nano-Structured Manganese Oxide as a Cathodic Catalyst for Enhanced Oxygen Reduction in a Microbial Fuel Cell Fed with a Synthetic Wastewater. *Water Res.* **2010**, *44*, 5298–5305. [[CrossRef](#)]
35. Cheng, S.; Liu, H.; Logan, B.E. Power Densities Using Different Cathode Catalysts (Pt and CoTMPP) and Polymer Binders (Nafion and PTFE) in Single Chamber Microbial Fuel Cells. *Environ. Sci. Technol.* **2005**, *40*, 364–369. [[CrossRef](#)]
36. Liu, H.; Logan, B.E. Electricity Generation Using an Air-Cathode Single Chamber Microbial Fuel Cell in the Presence and Absence of a Proton Exchange Membrane. *Environ. Sci. Technol.* **2004**, *38*, 4040–4046. [[CrossRef](#)]
37. Feng, Y.; Yang, Q.; Wang, X.; Logan, B.E. Treatment of Carbon Fiber Brush Anodes for Improving Power Generation in Air-Cathode Microbial Fuel Cells. *J. Power Sources* **2010**, *195*, 1841–1844. [[CrossRef](#)]
38. Zang, L.; Liu, C.; Zhuang, L.; Li, W.; Zhou, S.; Zang, J. Manganese Dioxide as an Alternative Cathodic Catalyst to Platinum in Microbial Fuel Cells. *Biosens. Bioelectron.* **2009**, *24*, 2825–2829. [[CrossRef](#)]
39. Córdoba-Torres, P. Relationship between Constant-Phase Element (CPE) Parameters and Physical Properties of Films with a Distributed Resistivity. *Electrochim. Acta* **2017**, *225*, 592–604. [[CrossRef](#)]
40. Landesfeind, J.; Pritzl, D.; Gasteirger, H.A. An Analysis Protocol for Three-Electrode Li-Ion Battery Impedance Spectra: Part I. Analysis of a High-Voltage Positive Electrode. *J. Electrochem. Soc.* **2017**, *164*, A1773. [[CrossRef](#)]
41. Teufl, T.; Pritzl, D.; Solchenbach, S.; Gasteirger, H.A.; Mendez, M.A. State of Charge Dependent Resistance Build-Up in Li-and Mn-Rich Layered Oxides during Lithium Extraction and Insertion. *J. Electrochem. Soc.* **2019**, *166*, A1275. [[CrossRef](#)]
42. Noori, M.T.; Ghangrekar, M.M.; Mukherjee, C.K.; Min, B. Biofouling Effects on the Performance of Microbial Fuel Cells and Recent Advances in Biotechnological and Chemical Strategies for Mitigation. *Biotechnol. Adv.* **2019**, *37*, 107420. [[CrossRef](#)] [[PubMed](#)]
43. Yesilbag, Y.O.; Tuzluca, F.N.; Ertugrul, M. The Use of  $\alpha$ -MnOOH Nanosheets as Battery-Type Electrode for Supercapacitor Applications. *J. Mater. Sci. Mater. Electron.* **2019**, *30*, 8201–8209. [[CrossRef](#)]

44. Majidi, M.R.; Shahbazi Farahani, F.; Hosseini, M.; Ahadzadeh, I. Low-Cost Nanowired  $\alpha$ -MnO<sub>2</sub>/C as an ORR Catalyst in Air-Cathode Microbial Fuel Cell. *Bioelectrochemistry* **2019**, *125*, 38–45. [[CrossRef](#)]
45. Xiong, Q.Q.; Xia, X.H.; Tu, J.P.; Chen, J.; Zhang, Y.Q.; Zhou, D.; Gu, C.D.; Wang, X.L. Hierarchical Fe<sub>2</sub>O<sub>3</sub>@Co<sub>3</sub>O<sub>4</sub> Nanowire Array Anode for High-Performance Lithium-Ion Batteries. *J. Power Sources* **2013**, *240*, 344–350. [[CrossRef](#)]
46. Sevda, S.; Chayambuka, K.; Sreekrishnan, T.R.; Pant, D.; Dominguez-Benetton, X. A Comprehensive Impedance Journey to Continuous Microbial Fuel Cells. *Bioelectrochemistry* **2015**, *106*, 159–166. [[CrossRef](#)] [[PubMed](#)]
47. Xochitl, D.B.; Sevda, S.; Vanbroekhoven, K.; Pant, D. The Accurate Use of Impedance Analysis for the Study of Microbial Electrochemical Systems. *Chem. Soc. Rev.* **2012**, *41*, 7228–7246. [[CrossRef](#)]
48. Wen, Q.; Wu, Y.; Zhao, L.X.; Sun, Q.; Kong, F.Y. Electricity Generation and Brewery Wastewater Treatment from Sequential Anode-Cathode Microbial Fuel Cell. *J. Zhejiang Univ. Sci. B* **2010**, *11*, 87–93. [[CrossRef](#)] [[PubMed](#)]
49. Mateo, S.; Mascia, M.; Fernandez-Morales, F.J.; Rodrigo, M.A.; Di Lorenzo, M. Assessing the Impact of Design Factors on the Performance of Two Miniature Microbial Fuel Cells. *Electrochim. Acta* **2019**, *297*, 297–306. [[CrossRef](#)]
50. Tremouli, A.; Antonopoulou, G.; Bebelis, S.; Lyberatos, G. Operation and Characterization of a Microbial Fuel Cell Fed with Pretreated Cheese Whey at Different Organic Loads. *Bioresour. Technol.* **2013**, *131*, 380–389. [[CrossRef](#)]
51. Yuan, H.; Hou, Y.; Abu-Reesh, I.M.; Chen, J.; He, Z. Oxygen Reduction Reaction Catalysts Used in Microbial Fuel Cells for Energy-Efficient Wastewater Treatment: A Review. *Mater. Horiz.* **2016**, *3*, 382–401. [[CrossRef](#)]

**Disclaimer/Publisher’s Note:** The statements, opinions and data contained in all publications are solely those of the individual author(s) and contributor(s) and not of MDPI and/or the editor(s). MDPI and/or the editor(s) disclaim responsibility for any injury to people or property resulting from any ideas, methods, instructions or products referred to in the content.